



Multiwavelength fluorescence lidar observations of fresh smoke plumes

Igor Veselovskii¹, Nikita Kasianik¹, Mikhail Korenskii¹, Qiaoyun Hu², Philippe Goloub², Thierry Podvin², Dong Liu³

¹*Prokhorov General Physics Institute of the Russian Academy of Sciences, Moscow, Russia.*

²*Univ. Lille, CNRS, UMR 8518 - LOA - Laboratoire d'Optique Atmosphérique, F-59650 Lille, France*

³*State Key Laboratory of Modern Optical Instrumentation, College of Optical Science and Engineering: International Research Center for Advanced Photonics, Zhejiang University, Hangzhou 310027, China*

Correspondence: Philippe Goloub (philippe.goloub@univ-lille.fr)

Abstract

A five-channel fluorescence lidar was developed for the study of atmospheric aerosol. The fluorescence spectrum induced by 355 nm laser emission is analyzed in five spectral intervals using interference filters. Central wavelengths and the widths of these five interference filters are respectively: 438/29, 472/32, 513/29, 560/40 and 614/54 nm. The relative calibration of these channels has been performed using a tungsten-halogen lamp with color temperature 2800K. This new lidar system was operated during Summer – Autumn 2022, when strong forest fires occurred in the Moscow region and generated a series of smoke plumes analyzed in this study. Our results demonstrate that, for urban aerosol, the maximal fluorescence backscattering is observed in 472 nm channel. For the smoke the maximum is shifted toward longer wavelengths, and the fluorescence backscattering coefficients in 472 nm, 513 nm and 560 nm channels have comparable value. Thus, from the analysis of the ratios of fluorescence backscattering in available channels, we show that it is possible to identify smoke layers. The particle classification based on single channel fluorescence capacity (ratio of the fluorescence backscattering to elastic one), has limitations at high relative humidity (RH). Fluorescence capacity is indeed decreasing when water uptake of particles enhances the elastic scattering. However, the spectral variation of fluorescence backscattering does not evidence any dependence on RH and can be therefore considered for aerosol identification.



1. Introduction

The knowledge of the chemical composition of atmospheric aerosol is important for characterization of its impact on the Earth radiation balance (Boucher et al., 2013; IPCC 2022). The composition of aerosol, however, is strongly variable, and in practice, several general aerosol types, usually, are considered, based on their origin (Dubovik et al., 2002). The Mie-Raman and high spectral resolution lidars provide the opportunity to derive vertical distribution of the particle extinction and backscattering coefficients together with multispectral depolarization ratio. Based on these observations the main aerosol types can be distinguished (Burton et al., 2012, 2013; Groß et al., 2013; Mamouri et al., 2017; Papagiannopoulos et al., 2018; Nicolae et al., 2018; Hara et al., 2018; Wang et al., 2021; Mylonaki et al., 2021). However, due to the variability of aerosol parameters, the particle intensive properties (properties that are independent on concentration), such as lidar ratios, depolarization ratios and Angstrom exponents can vary in a wide range, even for aerosols from the same origin, which complicates their identification.

The fluorescence measurements provide new independent information about aerosol composition, which can be used for classification. (Veselovskii et al., 2022b). Being induced by 355 nm laser radiation the atmospheric fluorescence emission spreads in a wide spectral range from approximately 380 nm to beyond 700 nm. The multianode photomultipliers combined with spectrometer, in principle, allow profiling the full fluorescence spectrum (Sugimoto et al., 2012; Saito et al., 2022; Reichardt et al., 2022). In a more simple approach a single fluorescence channel has been integrated into existing multiwavelength Mie-Raman lidar (Veselovskii et al., 2020), and a fraction of the fluorescence spectrum is selected by a wideband interference filter. High transmittance of modern interference filters (above 95%), allows efficient detection of fluorescence emission, and when combined with simultaneous depolarization measurements the main aerosol types, such as dust, smoke, pollen and urban can be identified (Veselovskii et al., 2022b). This classification scheme relies on the fluorescence capacity G_λ , which is the ratio of fluorescence backscattering to elastic backscattering at laser wavelength. The fluorescence capacity, however, depends on the relative humidity (RH), because enhanced elastic backscattering leads to decrease of G_λ (Veselovskii et al., 2021). Thus, at high RH, we cannot attribute unambiguously the decrease of G_λ to some water uptake to some changes in the aerosol composition.



63 The water uptake increases the elastic backscattering but normally does not alter the
64 chemical components thus, total amount of fluorescent molecules within a particle does not
65 change. The illumination intensity distribution within a particle, as well as the emission angular
66 distribution can be altered by the change of particle size and refractive index during the
67 hygroscopic growth. However, this effect occurs for relatively big microspheres with size
68 parameter exceeding approximately 10 (Veselovskii et al., 2002). Thus, fluorescence of the fine
69 mode particles should be less influenced by the hygroscopic growth. Our existing lidar data-base
70 in well mixed boundary layer situations demonstrate that, at least, for urban and smoke particles,
71 the fluorescence backscattering coefficient did not change during water uptake. Thus, we have
72 good reason to expect, that fluorescence spectrum is not modified by the aerosol hygroscopic
73 growth, and several fluorescence channels should provide more reliable information upon
74 aerosol type.

75 Smoke is one of the most abundant aerosol types and it was intensively studied with Mie-
76 Raman lidars for decades (Adam et al., 2021 and references therein). Smoke is characterized also
77 by high fluorescence capacity, thus fluorescence lidar measurements proved to be very efficient
78 for smoke identification and analysis (Hu et al., 2022, Veselovskii et al., 2022a,b). However, as
79 mentioned, at high RH classification of smoke, based on a single channel fluorescence may fail.
80 The solution could be the detection of fluorescence at several wavelengths. In July 2022 a new
81 lidar system equipped with five fluorescence channels, was assembled in Prokhorov General
82 Physics Institute, Troitsk, Moscow. The lidar was in operation during Summer and Autumn
83 2022, when strong forest fires occurred in the Moscow region. In this paper we analyze the
84 spectral dependence of the fluorescence backscattering inside and outside the smoke plumes. The
85 results demonstrate that the hygroscopic growth does not affect the spectral dependence of
86 fluorescence backscattering.

87

88 **2. Experimental setup**

89 The fluorescence lidar is based on a tripled Nd:YAG laser with pulse energy of 80 mJ at
90 355 nm and repetition rate of 20 Hz. Backscattered light is collected by a 40 cm aperture
91 Newtonian telescope and the lidar signals are digitized with Licel transient recorders with 7.5 m
92 range resolution, allowing simultaneous detection in the analog and photon counting modes. The
93 optical scheme of the receiving module is presented in Fig.1. The system is designed to detect



94 elastic backscattering at 355 nm, nitrogen Raman backscattering at 387 nm and fluorescence
 95 backscattering in five spectral intervals. These intervals are separated with dichroic beamsplitters
 96 and isolated by the interference filters manufactured by Alluxa. The central wavelengths and the
 97 widths of transmission bands (FWHM) of these fluorescence channels are respectively: 438/29,
 98 472/32, 513/29, 560/40 and 614/54 nm. The transmission of the filters exceeds 97%, while
 99 suppression of optical signal out of band is above OD6. To improve the suppression of elastic
 100 backscattering we installed two filters in tandem in every channel.

101 Laser radiation at 532 nm can induce additional aerosol fluorescence which will
 102 contaminate long-wave channels. To remove potential contamination, the emission at 532 nm
 103 and 1064 nm are separated with dichroic mirrors and redirected to an optical dump. Therefore,
 104 the laser beam sent into the atmosphere has only one wavelength - 355 nm. As follows from
 105 Fig.1, the 532 nm radiation is out of the transmission band of the filters, which prevents the
 106 leaking of residual 532 nm component to the fluorescence channels. We should mention, that the
 107 vibrational overtone of N₂ Raman scattering at 424.4 nm is within the transmission band of 438
 108 nm channel. In accordance with results of Knippers et al. (1985), Raman intensity of this
 109 overtone is about three orders lower than intensity of N₂ fundamental vibration (for 488 nm laser
 110 wavelength). Based on our measurements, contribution of N₂ overtone to fluorescence signal
 111 from urban aerosol (with backscattering coefficient of 1.0 Mm⁻¹sr⁻¹ at 355 nm and $G_{438}=0.3 \times 10^{-4}$
 112 ⁴) is estimated to be below 5% at 1000 m height. In all the channels the PMTs R9880U-01 were
 113 used, except in the 614 nm channel, where R9880-20 PMT was installed, due to its higher
 114 sensitivity in the red spectral region. The strong sunlight background at daytime restricts the
 115 fluorescence observations to only nighttime.

116 The aerosol extinction coefficients at 355 nm (α_{355}) were calculated from Raman
 117 observations as described in Ansmann et al., (1992). For calculation of backscattering coefficient
 118 β_{355} in the presence of clouds, this method was modified (Veselovskii et al, 2022b). Additional
 119 information about atmospheric properties was available from radiosonde measurements at
 120 Dolgoprudnyi station, located about 50 km away from the observation site. It should be
 121 mentioned that the current lidar configuration does not allow measurement of the depolarization
 122 ratio.

123 The fluorescence backscattering coefficient β_{FA} is calculated from the ratio of
 124 fluorescence signal to 387 nm nitrogen Raman signal, as described in Veselovskii et al. (2020).



One reminds that $\beta_{F\lambda}$ is the integral of fluorescence backscattering over the filter transmission band D_λ . For calculation of $\beta_{F\lambda}$ one needs to know the differential cross section of nitrogen Raman scattering, σ_R , and the relative sensitivity of the nitrogen and fluorescence detection channels. The value $\sigma_R=2.744 \cdot 10^{-30} \text{ cm}^2 \text{ sr}^{-1}$ at 355 nm was taken from Venable et al. (2011). Sensitivity of R9880U-01 photocathode in the 387 nm - 438 nm **range varies for less than 10%**, so we neglect this variation and calculate relative sensitivity of the PMTs as described in Veselovskii et al. (2020). The relative sensitivity of the rest of the fluorescence channels in respect to the 438 nm one, was calculated from laboratory measurements using a tungsten-halogen **lamp Thorlabs QTH10/M with color temperature 2800K as a source, assuming this source follows the Planck blackbody emission**. This procedure was performed once a week and variations of the calibration coefficients during August-September 2022 period were below 15%.

To compare $\beta_{F\lambda}$ at different fluorescence channels we compute the mean backscattering coefficients per elementary spectral interval, $B_\lambda = \frac{\beta_{F\lambda}}{D_\lambda}$, denoted as “fluorescence spectral backscattering coefficient”. The fluorescence capacity G_λ , which is the ratio of the fluorescence backscattering to the elastic one, in principle, can be calculated for any laser wavelength. In our previous studies we calculated G_λ with respect to β_{532} , however, in this work, it was calculated with respect to 355 nm $G_\lambda = \frac{\beta_{F\lambda}}{\beta_{355}}$, since 532 nm wavelength was not available. All $\beta_{F\lambda}$, G_λ and B_λ profiles presented in this work were smoothed with the Savitzky – Golay method, using a second order polynomial with 21 points in the window.

3. Measurements and analysis

In August 2022 numerous smoke layers originating from the forest fires in Ryazan region (about 160 km South – East of Moscow) were detected over the lidar station. The travel time of the layers was less than two days, thus smoke can be considered as fresh. The previous fluorescence studies of smoke plumes transported over Atlantic and including 466/44 nm **fluorescence measurements revealed that fluorescence capacity (calculated for β_{532}), in the absence of hygroscopic growth, varied within the range $(2.5-5.0) \times 10^{-4}$ (Veselovskii et al., 2021, 2022a,b; Hu et al., 2022).** The Backscattering Angstrom Exponent (BAE) of smoke for 355/532



nm wavelengths, is about 2.0, and fluorescence capacity G_{472} in 472/32 nm channel (calculated for β_{355}) is expected to be in the range $(0.8-1.6) \times 10^{-4}$. For urban aerosol corresponding G_{472} should be $(0.03-0.3) \times 10^{-4}$. Here and below the fluorescence capacity will be provided for 472 nm, because in most of the cases fluorescence in this channel was maximal.

157

3.1. Fluorescence measurements during smoke episode

27-28 August 2022

Two-day backward trajectories from the NOAA HYSPLIT model for the air mass reaching Moscow on 28 August at 00:00 UTC are shown in Fig.2. Air masses observed at 1500 m, passed over the fire region, close to the ground, and should thus contain products of biomass burning. The relative humidity measured by the radiosonde, at 00:00 UTC, was about 35% at 1000 m and increased with height up to 70% at 3000 m. Temporal evolution of the aerosol backscattering coefficient, β_{355} , fluorescence backscattering, β_{F438} , and fluorescence capacity, G_{472} , are shown in Fig.3. Aerosols are localized mainly below 3000 m, while above 4000 m cloud layers can be seen. In the boundary layer the fluorescence backscattering inside the boundary layer is the strongest before 20:30 UTC. The fluorescence capacity exceeds 2.5×10^{-4} , which is the highest observed G_{472} . After 20:30 G_{472} decreases but remains above 1.0×10^{-4} , which, in principle, can be due to mixing of smoke with urban aerosol.

Vertical profiles of the fluorescence spectral backscattering coefficients B_{λ} are shown in Fig.4 for the period corresponding to maximum fluorescence capacity (19:00-20:00 UTC). Profiles of B_{472} , B_{513} , B_{560} are similar, indicating that fluorescence does not demonstrate significant spectral variations in 472-560 nm spectral range. The fluorescence capacity G_{472} is above 2.0×10^{-4} , in 1.0 km – 2.5 km height range, where β_{355} and B_{λ} are maximum. The ratios B_{472}/B_{438} , B_{472}/B_{513} , B_{472}/B_{560} , B_{472}/B_{614} do not demonstrate height dependence in 1000-2500 m range, thus, the fluorescence spectrum in this interval is not changed. Fig.5 shows spectra of fluorescence for two distinct temporal intervals. In the interval corresponding to high fluorescence capacity (19:00-20:00 UTC), the maximum fluorescence backscattering is observed in 513 nm channel, which agrees with spectrum of smoke fluorescence provided by Reichard et al. (2022). In the second interval (23:00-01:00 UTC), when fluorescence capacity is lower, the fluorescence is maximal at 472 nm and at longer wavelengths it decreases fast. The lidar ratios (S_{355}) for both time intervals are shown in the same figure. For the first interval (with maximum



184 G_{472} S_{355} is about 60 sr, while for the second interval S_{355} decreases to about 40 sr. Lidar ratio 60
 185 sr is in agreement with S_{355} reported for fresh smoke (Adam et al., 2021), while values about 40
 186 sr are usually observed for urban particles at low RH. The highest spectral fluorescence capacity
 187 of smoke (capacity per elementary spectral interval), reported by Reichard et al. (2022) for 455–
 188 535 nm range is about $8 \times 10^{-6} \text{ nm}^{-1}$. This is very comparable with our value ($11 \times 10^{-6} \text{ nm}^{-1}$)
 189 calculated from data plotted in Fig.4 and 5 at 472 nm in 19:00-20:00 UTC time interval.

190 The variation of the fluorescence spectra with height is revealed by the ratio of the
 191 fluorescence backscattering coefficients at different wavelengths (e.g. B_{472}/B_{λ}). In particular,
 192 inside the aerosol plume in Fig.3 B_{λ} does not change significantly in 472 – 560 nm range, so the
 193 ratios B_{472}/B_{513} , B_{472}/B_{560} are close to 1.0. Temporal evolution of these ratios is shown in the right
 194 column in Fig.3. The intervals with the maximum G_{472} are well distinguished by minimum
 195 B_{472}/B_{513} and B_{472}/B_{560} ratios. At the same time, ratio B_{472}/B_{438} appears to be less sensitive to G_{472}
 196 changes. Actually, this ratio even increases inside the aerosol plume. Thus, the analysis of Fig.3
 197 reveals two types of the particles. The first type having a high fluorescence capacity
 198 ($G_{472} > 2.0 \times 10^{-4}$) and a lidar ratio close to 60 sr can be classified as “pure” smoke. The second
 199 type, with lower fluorescence capacity ($G_{472} \sim 1 \times 10^{-4}$) and a smaller lidar ratio, can be a mixture
 200 of smoke and urban aerosol.

201 Forest fires stopped in the beginning of September, so during September – October the
 202 urban aerosols were predominant. Fig.6 shows corresponding fluorescence spectra, normalized
 203 to B_{472} . Measurements were performed during 07:00-09:00 UTC and averaged within the
 204 boundary layer between 500 m and 1000 m. For urban aerosols, fluorescence at wavelengths
 205 larger than 472 nm decreases fast. Presence of remaining smoke, however, may lead to some
 206 increase of B_{λ} in the 513 – 614 nm interval. For urban aerosol particles the fluorescence capacity
 207 G_{472} for urban particles varied within $(0.1-0.4) \times 10^{-4}$ and the lidar ratios within 30-50 sr interval.
 208 Thus, a mixture of smoke and urban particles can explain the variability observed in fluorescence
 209 spectrum on Fig.5.

210

211 **17 August 2022**

212 The spatio – temporal intervals with high fluorescence capacity were observed also for
 213 other days. On August 17-18, 2022 between 18:00 – 19:00 UTC, fluorescence capacity at 472
 214 nm, the G_{472} , within the aerosol plume increased above 1.0×10^{-4} (Fig.7). Simultaneously, the



ratio B_{472}/B_{560} decreases to less than 0.8. Outside the plume, the fluorescence capacity is $(0.4-0.7) \times 10^{-4}$ and the ratio B_{472}/B_{560} increases up to 1.5. Corresponding fluorescence spectra are shown in Fig.8. Inside the plume the fluorescence is maximal in the 560 nm channel, while outside the maximum is shifted to 472 nm. Similarly to the 27-28 August event (Fig.5), the lidar ratio S_{355} is about 60 sr inside the plume and decreases down to about 30 sr outside the plume. Thus, again, we conclude that in the interval having the highest G_{472} , smoke particles are predominant, while outside we very likely addressed a mixture of smoke and urban aerosol.

3.2. Analysis of fluorescence profiles observed in the presence of hygroscopic growth of aerosol.

Our previous studies with a single channel fluorescence lidar revealed, that the hygroscopic growth of aerosol particles decreases the fluorescence capacity, but does not affect the fluorescence backscattering coefficient (Veselovskii et al, 2021). Thus, when fluorescence spectra are available, one can expect that spectral dependence of fluorescence backscattering coefficients will preserve information about particle type (will not be influenced by water uptake). Below, we provide interpretation of the measurements performed during the nights August 21-22 and 23-24 2022. In both cases, RH increased with altitude and the hygroscopic growth is one possible contributor to the observed increase of particle backscattering coefficient. Our results show, that on August 21-22 the shape of the fluorescence spectrum (the set of B_{λ}/B_{472} ratios) did not exhibit any change with altitude, whereas, conversely, on August 23-24 the shape of the fluorescence spectrum has changed with altitude, indicating possible change of aerosol composition with height.

Fig.9. shows vertical profiles of the fluorescence spectral backscattering coefficients, B_{λ} , together with backscattering β_{355} coefficient, fluorescence capacity G_{472} , and B_{472}/B_{438} , B_{472}/B_{513} , B_{472}/B_{560} ratios on August 21 2022. Profiles of B_{472}/B_{614} ratio are noisier and not used for analysis. The profile of relative humidity measured by a radiosonde at Dolgoprudnii station, shows increase of RH with altitude from 30% to 80% within 1000-4500 interval. Inside 3000-4000 m range, the fluorescence backscattering does not demonstrate significant variations while elastic backscattering increases by two orders of magnitude (from approximately $1 \text{ Mm}^{-1}\text{sr}^{-1}$ to $100 \text{ Mm}^{-1}\text{sr}^{-1}$), which should be attributed to aerosol hygroscopic growth. The fluorescence capacity, G_{472} , decreases to less than 0.01×10^{-4} at 4000 m, however, the ratios B_{472}/B_{438} ,



246 B_{472}/B_{513} , B_{472}/B_{560} do not change with altitude, meaning that i) the spectrum (its shape) is not
 247 affected by water uptake process and that ii) aerosol composition remains constant.

248 Temporal evolution of the particle parameters on the August 23-24 night is presented in
 249 Fig.10. The relative humidity increases with height and during 18:00-20:00 time interval a cloud
 250 was formed at ~3000 m. After 20:00 the fluorescence capacity inside 2000-3000 m height range
 251 is low (below 0.2×10^{-4}), however low values of G_{472} can also be explained by particle
 252 hygroscopic growth, thus one can not yet conclude that aerosol composition has changed,
 253 because the two effects (RH + aerosol changes) can occur simultaneously. Meanwhile, B_{472}/B_{560}
 254 ratio decreases above 2000 m, which can be an indication of aerosol composition change.
 255 Profiles of aerosol properties for the time interval 20:30-23:30 are shown in Fig.11. In
 256 accordance with the radiosonde measurements the relative humidity reaches 80% at 3000 m at
 257 00:00 UTC. At 1000 m height, where RH is low (~35%), G_{472} is about 0.4×10^{-4} , hence, urban
 258 aerosol type is predominant. Both B_{472}/B_{513} and B_{472}/B_{560} ratios decrease above 2000 m, while
 259 B_{472}/B_{438} increases. As mentioned above, such behavior can be an indication that contribution of
 260 smoke rises with height.

261 Normalized fluorescence spectra for two height intervals, 1000-1500 m and 2500-3000 m
 262 are shown in Fig.11c. In the second interval, the spectrum is shifted towards longer wavelengths,
 263 which corroborates that smoke fraction in the aerosol mixture increases above 2000 m. Thus, the
 264 analysis of this episode demonstrates that multi-spectral fluorescence backscattering provides
 265 opportunity for particle identification even in the presence of hygroscopic growth.

266

267 **Conclusions and perspectives**

268 Observations performed with a five-channel fluorescence lidar allow estimation of
 269 atmospheric aerosol fluorescence spectrum. For urban aerosol type the maximum of fluorescence
 270 is observed at 472 nm. However, for smoke particles, the maximum is shifted toward longer
 271 wavelengths and the fluorescence backscattering coefficients in the 472 nm, 513 nm and 560 nm
 272 channels are comparable. Hence, the ratios B_{472}/B_{513} or B_{472}/B_{560} , allow identification of the
 273 smoke layers because, for smoke, these ratios are smaller than for urban particles.

274 During strong forest fires in August 2022 we regularly observed over Moscow aerosol
 275 plumes, characterized by high fluorescence capacity ($G_{472} > 1.0 \times 10^{-4}$). Inside these plumes, lidar
 276 ratio S_{355} increased up to 60 sr simultaneously with a shift of the fluorescence maximum to 513



277 nm or 560 nm. Particles inside plume are very likely composed of “pure” smoke, while outside
 278 the plume, a smoke/urban mixture is probable. Classification of aerosol particles based on single
 279 channel fluorescence measurements has limitations at high RH because the fluorescence capacity
 280 is decreasing due to water uptake. However, our experimental database of fluorescence
 281 backscattering ratios does not evidence noticeable dependence with RH, which means these
 282 ratios allow us to identify smoke layers even in the presence of hygroscopic growth.

283 In our measurements, the laser emitted only 355 nm radiation, however, for aerosol
 284 detailed characterization it is important to use 532 nm and 1064 nm wavelengths as well. Such
 285 Laser Induced Fluorescence Exploratory instrument (LIFE) is currently under construction and
 286 will start operation in 2023, at LOA, ATOLL platform (France), in the frame of the OBS4CLIM
 287 project and AGORA-Lab research and development activities. More generally, it seems
 288 promising to upgrade widely-used multiwavelength Mie-Raman high performance lidars with a
 289 couple of fluorescence channels. According to our results, at least for smoke, the 472 nm and
 290 513 nm channels can be considered. The wavelengths of anti-Stokes components of nitrogen
 291 and oxygen stimulated by 532 nm radiation are 473 nm and 491 nm respectively. The oxygen
 292 component is blocked by the filter, while the nitrogen one is inside the transmission band of the
 293 472 nm channel. The power of anti-Stokes scattering increases with temperature, but even at
 294 30°C⁰ its contribution to the fluorescence signal is insignificant. Estimations show that for
 295 backscattering coefficient $\beta_{355}=1.0 \text{ Mm}^{-1}\text{sr}^{-1}$ and $\beta_{513}=0.2\times 10^{-4} \text{ Mm}^{-1}\text{sr}^{-1}$ (urban aerosol), the
 296 relative contribution of the nitrogen anti-Stokes component to the fluorescence at 1000 m height
 297 is below 4×10^{-4} .

298 The results presented in this study are preliminary. We focused mainly on the fresh
 299 smoke analysis. However, smoke particle fluorescence properties depend on its chemical
 300 composition, in particular, on its organic carbon fraction. In addition, smoke fluorescence may
 301 be influenced by the burning process and transportation conditions. Thus, fluorescence spectra
 302 appears to be a relevant information to differentiate fresh from aged smoke particles. More
 303 observation campaigns, at different locations, are needed to clarify this. In the coming Spring –
 304 Summer period analysis of fluorescence spectra of different aerosol types, in particular, the
 305 pollens, is planned. At present, the system used in this study is being modified to include
 306 depolarization capability.

307



308 **Data availability.** Lidar measurements are available upon request
309 (philippe.goloub@univ-lille.fr).

310
311 **Author contributions.** IV assembled the lidar and wrote the paper. NK and MK performed the
312 measurements. QH, and PG analyzed data and helped with paper preparation. TP helped with
313 lidar design, DL participated in paper preparation.
314 .

315 **Competing interests.** The authors declare that they have no conflict of interests.

316

317 **Acknowledgement**

318 Development of the lidar system was supported by Russian Science Foundation (project
319 21-17-00114). We acknowledge funding from the CaPPA project funded by the ANR through
320 the PIA under contract ANR-11-LABX-0005-01, the “Hauts de France” Regional Council
321 (project CLIMIBIO) and the European Regional Development Fund (FEDER). ESA/QA4EO
322 program is greatly acknowledged for support of observation activity at LOA as well as
323 OBS4CLIM Equipex project funded by ANR.

324



References

- Adam, M., Stachlewska, I. S., Mona, L., Papagiannopoulos, N., Bravo-Aranda, J. A., Sicard, M., Nicolae, D. N., Belegante, L., Janicka, L., Szczepanik, D., Mylonaki, M., Papanikolaou, C.-A., Siomos, N., Voudouri, K. A., Alados-Arboledas, L., Apituley, A., Mattis, I., Chaikovsky, A., Muñoz-Porcar, C., Pietruczuk, A., Bortoli, D., Baars, H., Grigorov, I., and Peshev, Z.: Biomass burning events measured by lidars in EARLINET – Part 2: Optical properties investigation, *Atmos. Chem. Phys. Discuss.*, <https://doi.org/10.5194/acp-2021-759>, in review, 2021.
- Ansmann, A., Riebesell, M., Wandinger, U., Weitkamp, C., Voss, E., Lahmann, W., and Michaelis, W.: Combined Raman elastic-backscatter lidar for vertical profiling of moisture, aerosols extinction, backscatter, and lidar ratio, *Appl. Phys. B*, 55, 18–28, 1992.
- Boucher, O., Randall, D., Artaxo, P., Bretherton, C., Feingold, G., Forster, P., Kerminen, V.-M., Kondo, Y., Liao, H., Lohmann, U., Rasch, P., Satheesh, S. K., Sherwood, S., Stevens, B., and Zhang, X. Y.: Clouds and Aerosols, in: *Climate Change 2013: The Physical Science Basis. Contribution of Working Group I to the Fifth Assessment Report of the Intergovernmental Panel on Climate Change*, edited by: Stocker, T. F., Qin, D., Plattner, G.-K., Tignor, M., Allen, S. K., Boschung, J., Nauels, A., Xia, Y., Bex, V., and Midgley, P. M., Cambridge University Press, Cambridge, United Kingdom and New York, NY, USA, 2013.
- Burton, S. P., Ferrare, R. A., Hostetler, C. A., Hair, J. W., Rogers, R. R., Obland, M. D., Butler, C. F., Cook, A. L., Harper, D. B., and Froyd, K. D.: Aerosol classification using airborne High Spectral Resolution Lidar measurements – methodology and examples, *Atmos. Meas. Tech.*, 5, 73–98, 2012. <https://doi.org/10.5194/amt-5-73-2012>
- Burton, S. P., Ferrare, R. A., Vaughan, M. A., Omar, A. H., Rogers, R. R., Hostetler, C. A., and Hair, J. W.: Aerosol classification from airborne HSRL and comparisons with the CALIPSO vertical feature mask, *Atmos. Meas. Tech.*, 6, 1397–1412, 2013. <https://doi.org/10.5194/amt-6-1397-2013>
- Dubovik, O., Holben, B. N., Eck, T. F., Smirnov, A., Kaufman, Y. J., King, M. D., Tanre, D., and Slutsker, I.: Variability of absorption and optical properties of key aerosol types observed in worldwide locations, *J. Atmos. Sci.*, 59, 590–608, 2002.



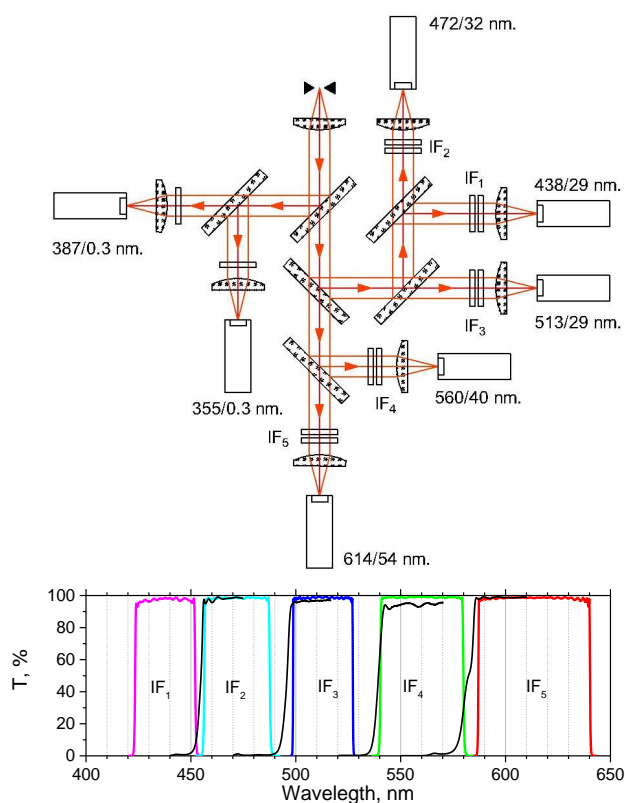
- 354 Groß, S., Esselborn, M., Weinzierl, B., Wirth, M., Fix, A., and Petzold, A.: Aerosol classification
 355 by airborne high spectral resolution lidar observations, *Atmos. Chem. Phys.*, 13, 2487–2505,
 356 2013. <https://doi.org/10.5194/acp-13-2487-2013>
- 357 Hara, Y., Nishizawa, T., Sugimoto, N., Osada, K., Yumimoto, K., Uno, I., Kudo, R., and
 358 Ishimoto, H.: Retrieval of aerosol components using multi-wavelength Mie-Raman lidar and
 359 comparison with ground aerosol sampling, *Remote Sens.*, 10, 937, 2018.
 360 <https://doi.org/10.3390/rs10060937>
- 361 Hu, Q., Goloub, P., Veselovskii, I., and Podvin, T.: The characterization of long-range
 362 transported North American biomass burning plumes: what can a multi-wavelength Mie-
 363 Raman-polarization-fluorescence lidar provide? *Atmos. Chem. Phys.* 22, 5399–5414, 2022
 364 <https://doi.org/10.5194/acp-22-5399-2022>
- 365 Knippers, W., van Helvoort, K., and Stolte, S.: Vibrational overtones of the homonuclear
 366 diatomics (N₂, O₂, D₂) observed by the spontaneous 385 Raman effect, *Chem. Phys. Lett.*,
 367 121, 279–286, 1985. [https://doi.org/10.1016/0009-2614\(85\)87179-7](https://doi.org/10.1016/0009-2614(85)87179-7)
- 368 Mamouri, R.-E., and Ansmann, A.: Potential of polarization/Raman lidar to separate fine dust,
 369 coarse dust, maritime, and anthropogenic aerosol profiles, *Atmos. Meas. Tech.*, 10, 3403–
 370 3427, 2017. <https://doi.org/10.5194/amt-10-3403-2017>
- 371 Mylonaki, M., Giannakaki, E., Papayannis, A., Papanikolaou, C.-A., Komppula, M., Nicolae, D.,
 372 Papagiannopoulos, N., Amodeo, A., Baars, H., and Soupiona, O.: Aerosol type classification
 373 analysis using EARLINET multiwavelength and depolarization lidar observations, *Atmos.*
 374 *Chem. Phys.*, 21, 2211–2227, 2021. <https://doi.org/10.5194/acp-21-2211-2021>
- 375 Nicolae, D., Vasilescu, J., Talianu, C., Biniotoglou, I., Nicolae, V., Andrei, S., and Antonescu,
 376 B.: A neural network aerosol-typing algorithm based on lidar data, *Atmos. Chem. Phys.*, 18,
 377 14511–14537, 2018. <https://doi.org/10.5194/acp-18-14511-2018>
- 378 Papagiannopoulos, N., Mona, L., Amodeo, A., D’Amico, G., Gumà Claramunt, P., Pappalardo,
 379 G., Alados-Arboledas, L., Guerrero-Rascado, J. L., Amiridis, V., Kokkalis, P., Apituley, A.,
 380 Baars, H., Schwarz, A., Wandinger, U., Biniotoglou, I., Nicolae, D., Bortoli, D., Comerón, A.,
 381 Rodríguez-Gómez, A., Sicard, M., Papayannis, A., and Wiegner, M.: An automatic
 382 observation-based aerosol typing method for EARLINET, *Atmos. Chem. Phys.*, 18, 15879–
 383 15901, 2018. <https://doi.org/10.5194/acp-18-15879-2018>



- Reichardt, J., Behrendt, O., and Lauermann, F.: Spectrometric fluorescence and Raman lidar: absolute calibration of aerosol fluorescence spectra and fluorescence correction of humidity measurements, *Atmos. Meas. Tech.*, 16, 1–13, 2023. <https://doi.org/10.5194/amt-16-1-2023>
- Saito, Y., Hosokawa, T., Shiraishi, K.: Collection of excitation-emission-matrix fluorescence of aerosol-candidate-substances and its application to fluorescence lidar monitoring, *Appl. Opt.*, 61, 653 – 660, 2022.
- Sugimoto, N., Huang, Z., Nishizawa, T., Matsui, I., Tatarov, B.: Fluorescence from atmospheric aerosols observed with a multichannel lidar spectrometer, *Opt. Expr.* 20, 20800-20807, 2012.
- Venable, D. D., Whiteman, D. N., Calhoun, M. N., Dirisu, A.O., Connell, R. M., Landulfo, E.: Lamp mapping technique for independent determination of the water vapor mixing ratio calibration factor for a Raman lidar system, *Appl. Opt.*, 50, 4622 - 4632, 2011.
- Veselovskii, I., Griaznov, V., Kolgotin, A., Whiteman, D.: “Angle- and size-dependent characteristics of incoherent Raman and fluorescent scattering by microspheres 2.: Numerical simulation”, *Appl. Opt.* 41, 5783-5791, 2002
- Veselovskii, I., Hu, Q., Goloub, P., Podvin, T., Korenskiy, M., Pujol, O., Dubovik, O., Lopatin, A.: Combined use of Mie-Raman and fluorescence lidar observations for improving aerosol characterization: feasibility experiment, *Atm. Meas. Tech.*, 13, 6691–6701, 2020. doi.org/10.5194/amt-13-6691-2020.
- Veselovskii, I., Hu, Q., Goloub, P., Podvin, T., Choël, M., Visez, N., and Korenskiy, M.: Mie–Raman–fluorescence lidar observations of aerosols during pollen season in the north of France, *Atm. Meas. Tech.*, 14, 4773–4786, 2021. doi.org/10.5194/amt-14-4773-2021
- Veselovskii, I., Hu, Q., Ansmann, A., Goloub, P., Podvin, T., Korenskiy, N.: Fluorescence lidar observations of wildfire smoke inside cirrus: A contribution to smoke-cirrus - interaction research, *Atmos. Chem. Phys.*, 22, 5209–5221, 2022a. <https://doi.org/10.5194/acp-22-5209-2022a>.
- Veselovskii, I., Hu, Q., Goloub, P., Podvin, T., Barchunov, B., and Korenskiy, M.: Combining Mie–Raman and fluorescence observations: a step forward in aerosol classification with lidar technology, *Atmos. Meas. Tech.*, 15, 4881–4900, 2022b. <https://doi.org/10.5194/amt-15-4881-2022>.
- Wang, N., Shen, X., Xiao, D., Veselovskii, I., Zhao, C., Chen, F., Liu, C., Rong, Y., Ke, J., Wang, B., Qi, B., Liu, D.: Development of ZJU high-spectral-resolution lidar for aerosol and cloud:



415 feature detection and classification, Journal of Quantitative Spectroscopy & Radiative
416 Transfer, v.261, 107513, 2021. doi.org/10.1016/j.jqsrt.2021.107513
417
418



419

420

421 Fig.1. Optical scheme of the receiving module of the lidar together with transmissions of
 422 interference filters IF₁-IF₅ in the fluorescence channels. Black lines show the transmissions of the
 423 45 degree dichroic beam splitters used for separation of fluorescence spectral components.

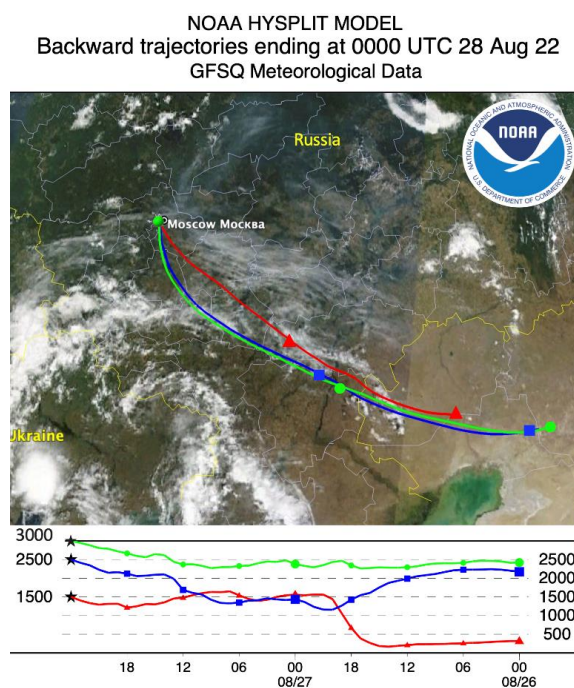
424



425

426

427



428

429

430 Fig.2. Two-day backward trajectories from the NOAA HYSPLIT model for the air mass in
 431 Moscow on 28 August at 00:00 UTC. The basemap is the Earth's true color image observed by
 432 MODIS Terra for the same period.

433



434

435

436

437

438

439

440

441

442

443

444

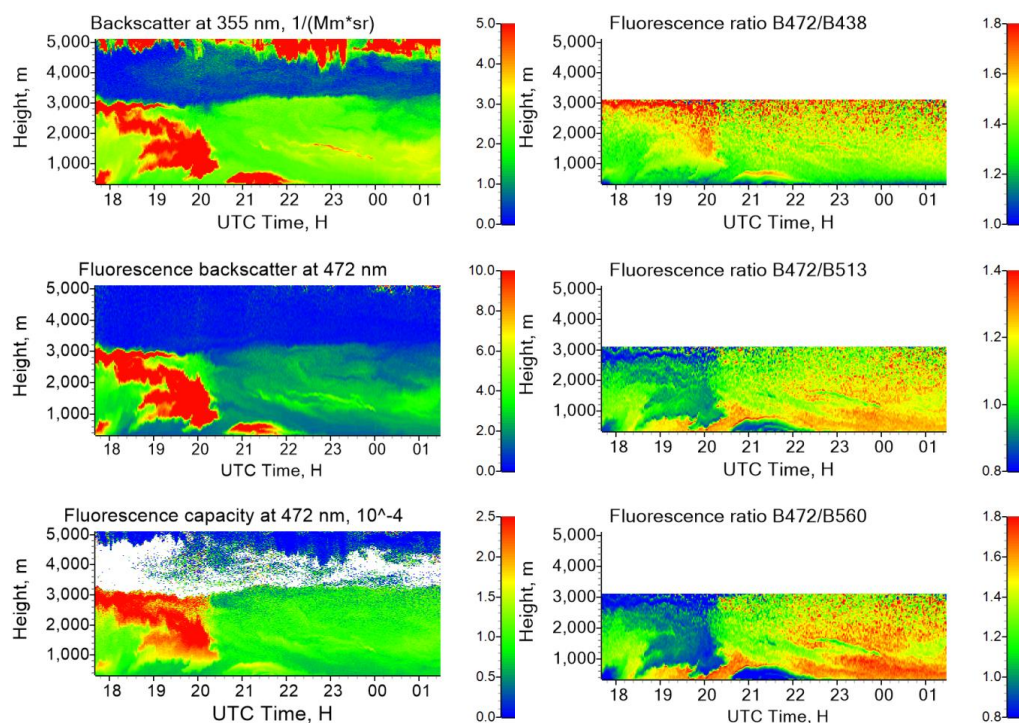


Fig.3. Spatio – temporal distribution of particle parameters on the night 27-28 August 2022. (left column) Aerosol backscattering coefficient β_{355} , fluorescence backscattering β_{F472} (in $10^{-4} \text{ Mm}^{-1} \text{sr}^{-1}$), fluorescence capacity G_{472} . (right column) Ratios of fluorescence spectral backscattering coefficients B_{472}/B_{438} , B_{472}/B_{513} , B_{472}/B_{560} .

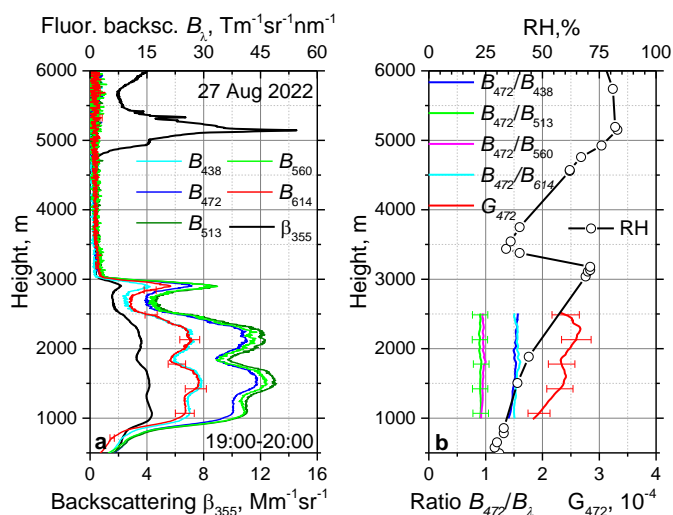


Fig.4. Observations on 27 August 2022 for period 19:00-20:00 UTC. (a) Fluorescence spectral backscattering coefficients B_λ at 438, 472, 513, 560, 614 nm and the aerosol backscattering coefficient β_{355} . (b) The ratios B_{472}/B_{438} , B_{472}/B_{513} , B_{472}/B_{560} , B_{472}/B_{614} and the fluorescence capacity G_{472} . Symbols show the relative humidity measured by a radiosonde at 00:00 UTC on 28 August.

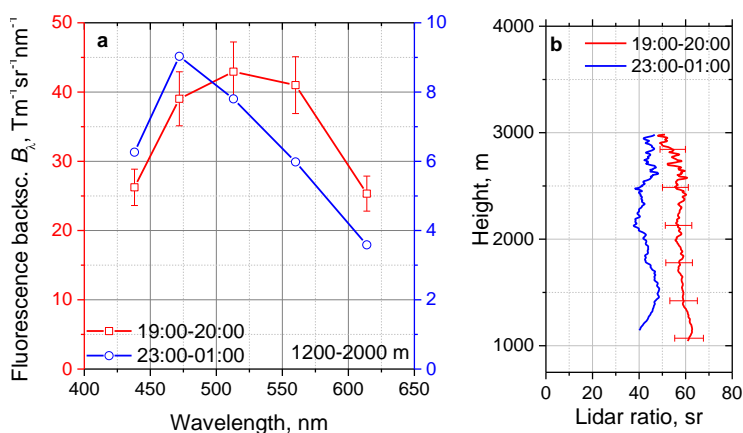
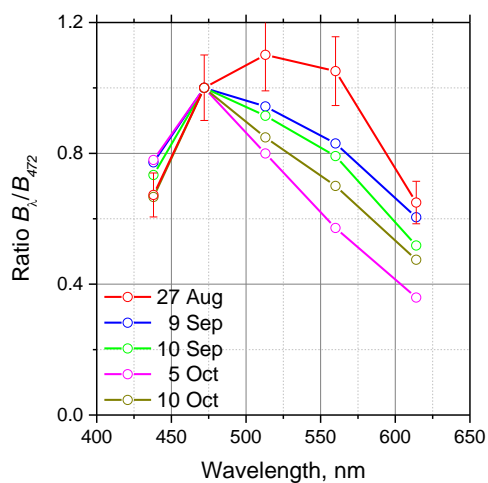


Fig.5. (a) Spectrum of fluorescence backscattering B_λ on the night 27-28 August 2022 for 19:00-20:00 and 23:00-01:00 UTC intervals. Results are averaged inside 1200-2000 m height range. (b) Profiles of lidar ratios at 355 nm for the same temporal intervals.



456



457

458 Fig.6. Fluorescence spectra measured in September - October 2022, when forest fires were over.

459 Fluorescence backscattering coefficients B_λ were averaged inside 500 – 1000 m height range and

460 normalized on B_{472} . For comparison, the fluorescence spectrum in smoke plume on 27 August

461 from Fig.5 is also presented.

462

463

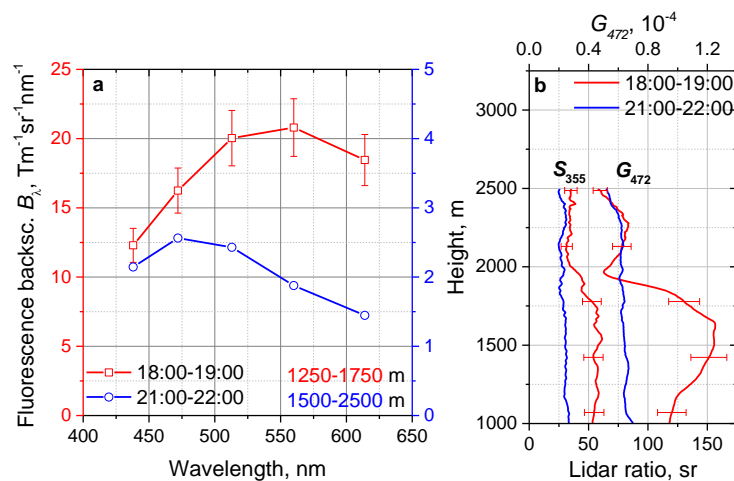
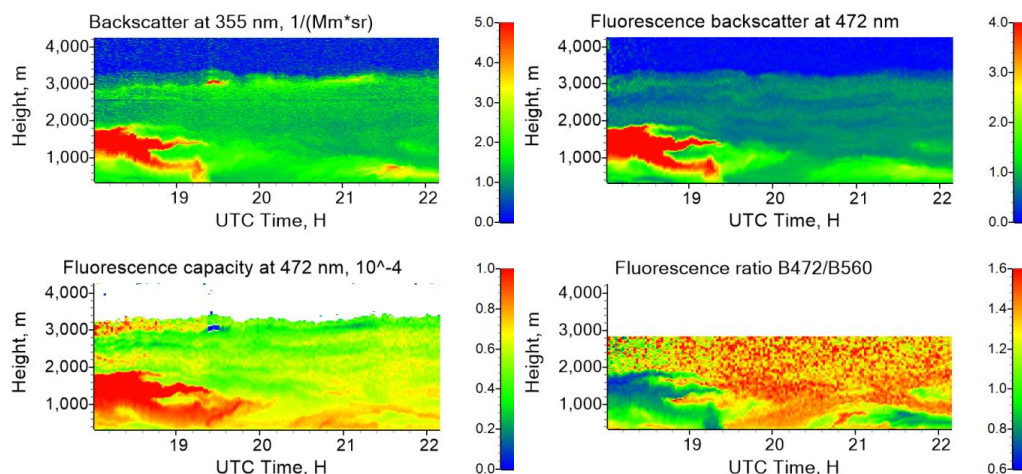


464

465

466

467 Fig.7. Observations on 17 August 2022. (left column) Aerosol backscattering coefficient β_{355}
 468 and fluorescence capacity G_{472} . (right column) Fluorescence backscattering coefficient β_{F472} (in
 469 $10^{-4} \text{ Mm}^{-1} \text{ sr}^{-1}$) and the ratio of fluorescence spectral backscattering coefficients B_{472}/B_{560} .
 470



471

472 Fig.8. (a) Spectra of fluorescence backscattering B_{λ} on 17 August 2022 for 18:00-19:00 UTC and
 473 21:00-22:00 UTC periods. Results are averaged within 1250-1750 m and 1500-2500 m height
 474 ranges respectively. (b) Profiles of lidar ratio S_{355} and fluorescence capacity G_{472} for the same
 475 temporal periods.

476

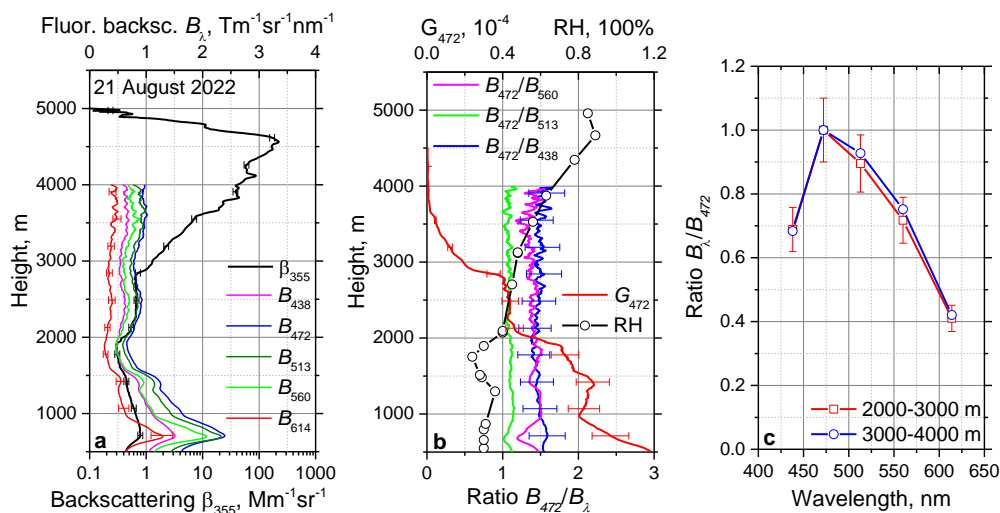


Fig.9. Vertical profiles of the particle parameters on 21 August 2022 for period 22:00-24:00 UTC. (a) The fluorescence spectral backscattering coefficients B_λ at 438, 472, 513, 560, 614 nm and the aerosol backscattering coefficient β_{355} . (b) The ratios B_{472}/B_{438} , B_{472}/B_{513} , B_{472}/B_{560} and the fluorescence capacity G_{472} . Symbols show the relative humidity measured by a radiosonde at 00:00 UTC on 22 August. (c) Spectrum of the fluorescence backscattering coefficient B_λ for height intervals 2000-3000 m and 3000-4000 m. Values of B_λ are normalized on B_{472} .

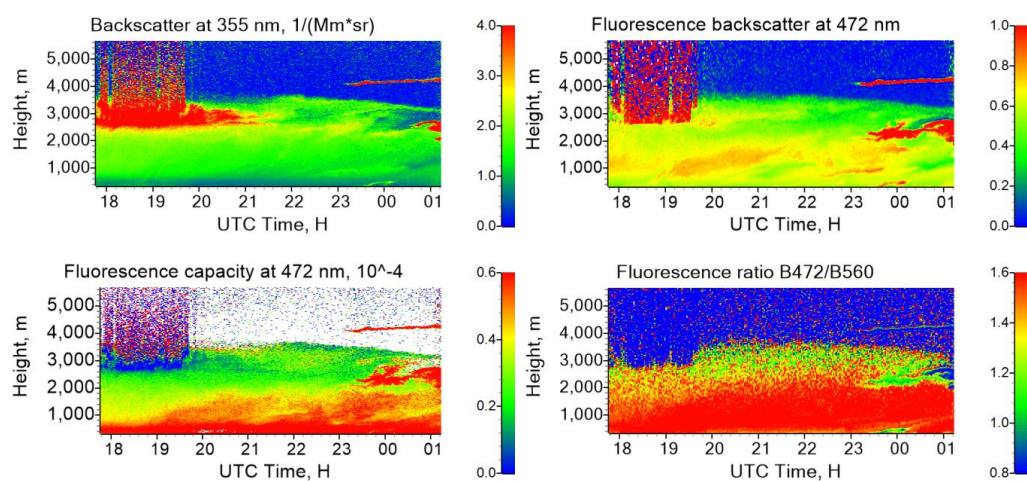
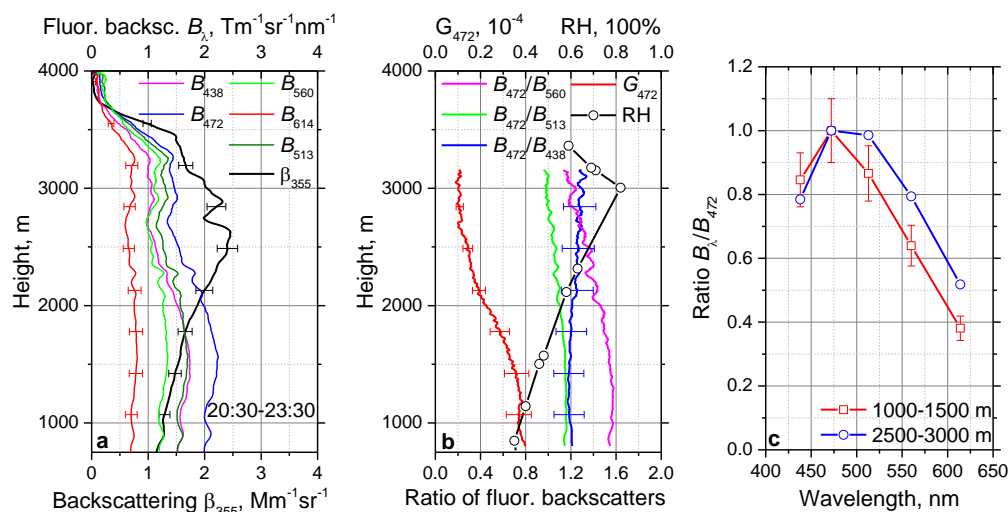


Fig.10. Spatio-temporal distributions of the particle parameters on the night 23-24 August 2022.
 (left column) The aerosol backscattering coefficient β_{355} together with the fluorescence capacity
 G_{472} . (right column) The fluorescence backscattering coefficient β_{F472} (in $10^{-4} \text{ Mm}^{-1} \text{ sr}^{-1}$) and the
 ratio B_{472}/B_{560} .



494



495

496

497 Fig.11. Vertical profiles of the particle parameters on 23 August 2022 for period 20:30-23:30
 498 UTC. (a) The fluorescence spectral backscattering coefficients B_λ at 438, 472, 513, 560, 614 nm
 499 and the aerosol backscattering coefficient β_{355} . (b) The ratios B_{472}/B_{438} , B_{472}/B_{513} , B_{472}/B_{560} and
 500 the fluorescence capacity G_{472} . Symbols show the relative humidity measured by a radiosonde at
 501 00:00 UTC on 24 August. (c) Spectrum of the fluorescence backscattering coefficient B_λ for
 502 height intervals 1000-1500 m and 2500-3000 m. Values of B_λ are normalized on B_{472} .

503

504